Harmonic Generation and Inverse Cascade in the z-Pinch Driven, Preseeded Multimode, Magneto-Rayleigh-Taylor Instability

D. E. Ruiz,[1,*] D. A. Yager-Elorriaga,[1] K. J. Peterson,[1] D. B. Sinars,[1] M. R. Weis,[1] D. G. Schroen,[2] K. Tomlinson,[2]
J. R. Fein,[1] and K. Beckwith[1]
[1]*Sandia National Laboratories, P.O. Box 5800, Albuquerque, New Mexico 87185-1186, USA*
[2]*General Atomics, San Diego, California 92121, USA*

(Received 21 October 2021; revised 21 March 2022; accepted 21 April 2022; published 21 June 2022)

The magneto-Rayleigh-Taylor instability (MRTI) plays an essential role in astrophysical systems and in magneto-inertial fusion, where it is known to be an important degradation mechanism of confinement and target performance. In this Letter, we show for the first time experimental evidence of mode mixing and the onset of an inverse-cascade process resulting from the nonlinear coupling of two discrete preseeded axial modes (400- and 550-μm wavelengths) on an Al liner that is magnetically imploded using the 20-MA, 100-ns rise-time Z Machine at Sandia National Laboratories. Four radiographs captured the temporal evolution of the MRTI. We introduce a novel unfold technique to analyze the experimental radiographs and compare the results to simulations and to a weakly nonlinear model. We find good quantitative agreement with simulations using the radiation magnetohydrodynamics code HYDRA. Spectral analysis of the MRTI time evolution obtained from the simulations shows evidence of harmonic generation, mode coupling, and the onset of an inverse-cascade process. The experiments provide a benchmark for future work on the MRTI and motivate the development of new analytical theories to better understand this instability.

DOI: 10.1103/PhysRevLett.128.255001

Introduction.—The magneto-Rayleigh-Taylor instability (MRTI) [1,2] is a ubiquitous phenomenon in astrophysics [3,4]. It plays an important role in the development of plumes in solar prominences [5] and filaments in the solar corona [6] and in the Crab Nebula [7,8]. This instability is also important in laboratory pinch plasmas such as those in magneto-inertial fusion, wire-array z-pinches, and equation-of-state studies [9–11]. In these applications, the MRTI occurs when a load plasma (which acts as a heavy fluid) is accelerated by a magnetic pressure (which acts as a light fluid). Like the classical Rayleigh-Taylor instability (RTI), this configuration is unstable [12]. In the case of the Magnetized Liner Inertial Fusion (MagLIF) platform [13–16], which uses high magnetic pressures to compress a fuel plasma to thermonuclear conditions, the MRTI can compromise the inertial confinement and degrade performance of MagLIF implosions [17].

The MRTI in laboratory z-pinch plasmas includes several physical effects that are absent in the classical RTI, for example, convergent imploding geometry, liner shells with finite thickness, inhomogeneities in the magnetic pressure, magnetic diffusion, Ohmic heating of the materials, and ablation. Several experiments have been published studying the MRTI growth on the 100-ns timescale. For example, single-mode seeded MRTI experiments were reported in Refs. [18,19]. Unseeded MRTI growth was investigated in cylindrical liners [20,21] and planar slabs [22]. Helical MRTI modes spontaneously emerge in smooth cylindrical loads when applying an axial magnetic field [23–26], which demonstrates the importance of magnetic tension effects unique to the MRTI.

This Letter presents a series of experiments investigating the growth and interaction of two MRTI modes initially seeded on the outer surface of an imploding shell. Experimental radiographs show evidence that a finite number of discrete initial modes lead to nonlinear harmonic generation and an inverse-cascade process, i.e., the transfer of energy from small to large scales, as was predicted previously [27]. We obtain good agreement when comparing the radiographs to those found using the radiation magnetohydrodynamics code HYDRA [28,29]. To quantitatively compare the experimental results to simulations and to a weakly nonlinear model, we develop a novel technique that uncovers the underlying transmission contours of the experimental radiographs accounting for the nonzero probing angle of the x-ray backlighter diagnostic.

Experiment setup.—Cylindrical liners were imploded using the 20-MA, 100-ns rise-time Z Machine at Sandia National Laboratories. The liners were made of Al-1100 alloy and were placed inside an eight-post, 26-mm inner-diameter return-current structure. The outer surfaces of the liners were machined with two periodic perturbations so that the initial outer radius was

$$R(z) = R_0 + A_0[\cos(k_1 z) + \cos(k_2 z) - 2], \tag{1}$$

0031-9007/22/128(25)/255001(6)

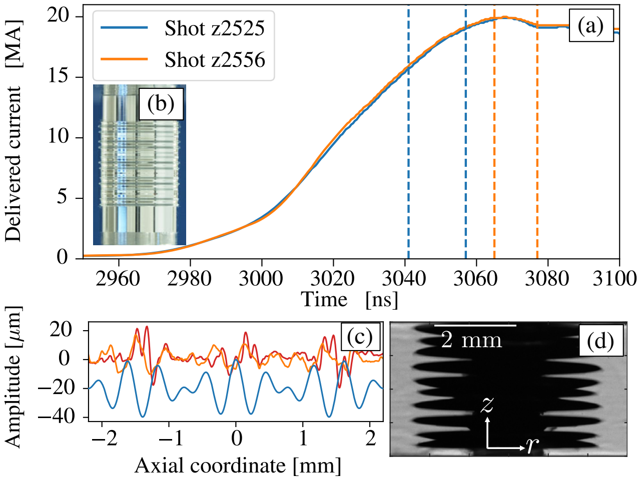

FIG. 1. (a) Delivered current with radiograph times overlaid as vertical bars. (b) Photograph of the liner with machined perturbations. (c) Blue: nominal perturbation in Eq. (1). Red and orange: surface deviations [magnified by 10(×)] of machined targets z2525 and z2556 measured by Coherence Scanning Interferometry. (d) Experimental radiograph at 3077 ns.

where $R_0 = 3.168$ mm is the unperturbed outer radius, $k_i \doteq 2\pi/\lambda_i$ are the mode wave numbers, and z is the axial coordinate. The wavelengths of the two initial modes were $\lambda_1 = 550\ \mu$m and $\lambda_2 = 400\ \mu$m, which correspond to $\bar{k}_1 \doteq k_1/(2\pi) = 18.1\ \mathrm{cm}^{-1}$ and $\bar{k}_2 \doteq k_2/(2\pi) = 25\ \mathrm{cm}^{-1}$, respectively. Both modes had the same initial amplitude $A_0 = 10\ \mu$m. (The instability starts in the linear growth regime.) Preshot characterization of the outer surfaces of the liners showed that local deviations from Eq. (1) did not exceed 2.0 μm along the field of view of the instrument (see Fig. 1). The inner radius of the targets was 2.876 mm. An on-axis, 1-mm-radius tungsten rod was fielded to limit self-emission radiation at stagnation.

Experiment results.—The MRTI evolution was diagnosed using a two-frame, 2-ns pulse-width monochromatic 6.151-keV backlighting diagnostic with 15-μm resolution [30]. Four radiographs were taken at $t = \{3041, 3057, 3065, 3077\}$ ns in two experimental shots (z2525 and z2556). The shot-to-shot difference between the measured currents was less than 2%. The cross-timing error between the radiographs and the measured currents is ±1 ns. The magnification error of the images is ±3% and can vary shot to shot. The radiograph backlighter has ±3° viewing angles for the first and second frame of each shot. Figure 1 shows a raw radiograph obtained at 3077 ns. The perturbations were azimuthally correlated with small differences appearing near the MRTI bubbles (innermost radial perturbations).

Simulations.—To help interpret the experimental data, we performed simulations using HYDRA, a massively parallel arbitrary Lagrangian-Eulerian radiation, resistive-diffusion, magnetohydrodynamics code [28,29]. HYDRA is one of the main design codes for MagLIF experiments [31–33]. The simulations were done in 2D rz cylindrical geometry. Radiation was modeled using multigroup diffusion. For the Al material properties, we used the LEOS equation-of-state table 130 [34] and the quantum Lee-More-Desjarlais conductivity table 29373 [35]. The simulation had initial resolution of 10.1 and 2.1 μm in the axial and radial directions, respectively. The runs were driven using the currents in Fig. 1.

Comparison of experiments and simulations.—Figure 2 compares enlarged images of the experimental radiographs and the synthetic radiographs generated from HYDRA simulations. The simulations reproduce the large-scale features of the experimental radiographs, particularly the shape and orientation of the bubbles and spikes. Note that the last radiography frame shows some bubble regions already colliding with the coaxial tungsten rod.

Small-scale discrepancies appear in Fig. 2. The plasma jets near the bubble regions at 3057 and 3065 ns likely originate from the surface roughness of the Al alloy, micron-scale scratches, pits, or metallic inclusions [36]. All can seed the electrothermal instability (ETI) [37] and lead to a local enhancement of Ohmic heating and ablation of the liner surface [38–41]. In the last two radiographs, the differences appearing near the bubble regions may be due to the ETI and machining imperfections of the liners. In Fig. 1, the largest measured deviations for the z2556 load were 1–2 μm in size and were located near the valley regions of the nominal perturbation. When initializing the simulations with the experimentally measured liner surfaces, we obtained minor qualitative improvements in the MRTI evolution (not shown).

To find the underlying transmission contour without the ±3° viewing-angle effect, we used a novel unfolding technique that models the plasma as a series of coaxial, opaque disks of radius R_j located at $z = Z_j$. When tilted by an angle θ, a disk contour becomes an ellipse obeying $(r/R_j)^2 + [(z - Z_j)/(R_j \sin\theta)]^2 = 1$. For each disk, R_j is the maximum radius such that the corresponding ellipse lies within the 25%-transmission contour of a given radiograph. The unfolded contour without viewing-angle effects is found using $R_{\mathrm{unfold}}(Z_j) = R_j$. We tested this unfold technique against simulations and found good agreement for cases with small MRTI growth. (Unfolded contours are overlaid on top of the simulated density plots in Fig. 4.) However, this analysis technique breaks down when the MRTI becomes large or when a single-valued function cannot represent the plasma contour.

The unfolded contours of the experimental radiographs are nonperiodic within the field of view. To make a quantitative comparison to the unfolded contours of the simulations, we used a least-squares spectral analysis (LSSA) technique to calculate the corresponding Fourier spectra [42,43]. For the LSSA, we used sine and cosine functions resulting from one to four mode combinations of the mother k_1 and k_2 modes that are expected from weakly nonlinear (WNL) theory [44–47]. Twenty modes were

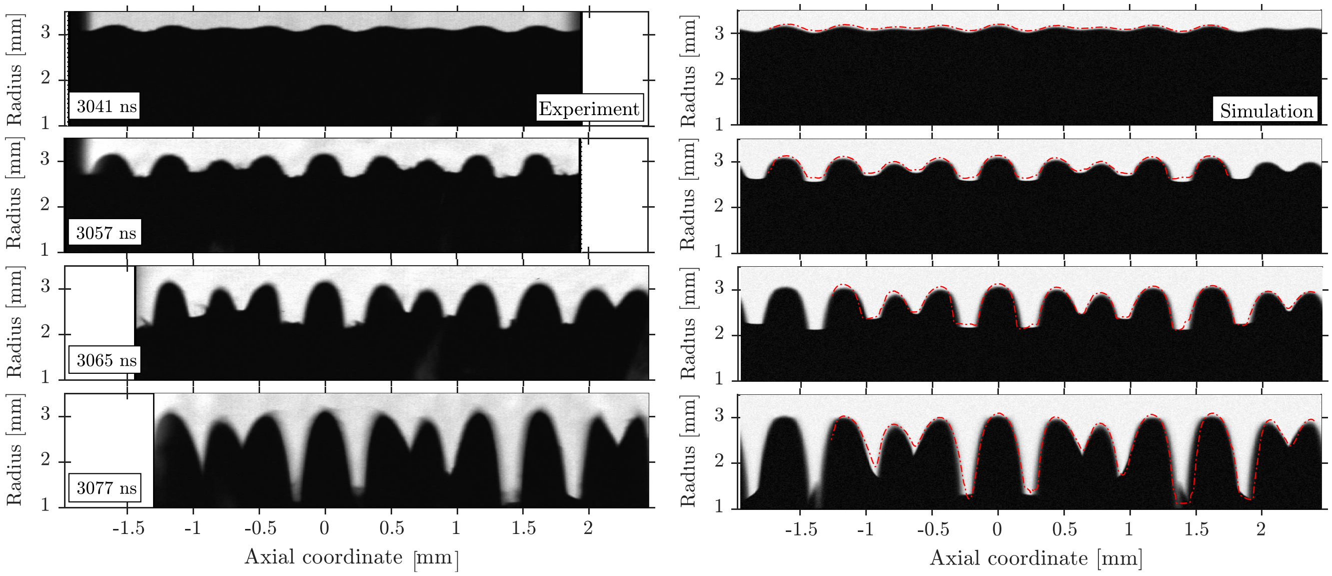

FIG. 2. Left column: enlarged images of the obtained experimental radiographs. The diagnostic has a 4-mm axial field of view. Right column: synthetic radiographs obtained from HYDRA using the initial perturbation in Eq. (1). The radiographs were calculated using the cold opacity of Al at 6.151 keV (102.6 cm^2/g). The 25%-transmission contours of the experimental radiographs are overlaid in red. Good qualitative agreement is obtained.

included, and the maximum wave number allowed was $4\bar{k}_2 = 100\ \mathrm{cm}^{-1}$. Figure 3 compares the LSSA spectra of the unfolded contours of the radiographs taken at $t = 3065$ ns (before the inner portions of the liner have collided with the central rod). Quantitative agreement is found for the largest amplitude modes. The mother k_1 and k_2 modes have, respectively, grown to 250 and 330 μm in amplitude, which correspond to growth factors of 25(×) and 33(×) of their initial amplitudes ($A_0 = 10\ \mu$m). Figure 3 shows harmonic generation of new daughter modes. The amplitudes of several daughter modes are larger than the initial amplitude of the mother modes. Notably, the $k_2 - k_1$ mode has the largest amplitude of the daughter modes and provides experimental evidence for the onset of transfer of energy from small scales to large scales, i.e., an inverse cascade occurring from the nonlinear coupling of discrete initial MRTI modes.

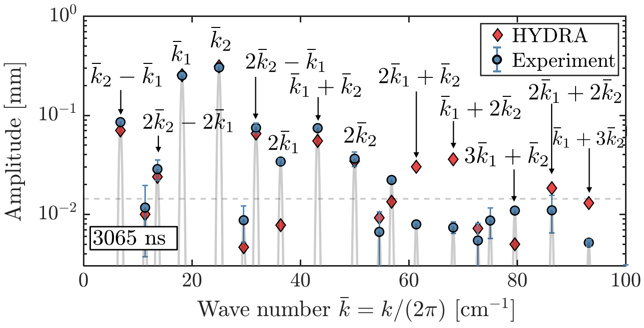

FIG. 3. LSSA amplitudes (in logarithmic scale) of the unfolded transmission contours inferred from the radiographs at 3065 ns. Blue error bars correspond to differences between the left- and right-hand sides of the experiment radiographs. Horizontal gray dashed line indicates the amplitude that can be measured to 30% uncertainty due to the fitting error.

Discussion of MRTI dynamics.—Figure 4 shows the time evolution of the liner density and of the Fourier spectrum of the liner mass per unit length $\hat{m}(t,z) \doteq 2\pi\int_0^\infty \rho(t,r,z)rdr$. At 3041 ns, the amplitudes of the k_1 and k_2 modes have increased 4(×) and 5(×), respectively, compared to their initial values (5.34 mg/cm) [48]. The k_2 mode grows faster than the k_1 mode since the linear MRTI growth rate increases with wave number: $\gamma_k(t) \simeq (k|\ddot{R}|)^{1/2}$, where $\ddot{R}(t)$ is the liner acceleration. The spectrum shows harmonic generation of new modes with wave numbers $k_2 - k_1$, $2k_1$, $k_1 + k_2$, and $2k_2$. These are "first-generation" daughter modes since they are the first modes expected to appear from the mother k_1 and k_2 modes in WNL RTI theory [44–47]. At 3057 ns, the spectrum shows new "second-generation" daughter modes. For example, to lowest order, the daughter $k_1 + 2k_2$ mode can appear from the coupling of the $(k_1, 2k_2)$ or $(k_2, k_1 + k_2)$ modes. At 3065 ns, the MRTI has entered the nonlinear phase with the maximum peak-to-peak amplitude of the perturbations being ~0.7 mm. The k_2 mode, which previously had the largest amplitude, is now smaller than the k_1 mode. The second-harmonic $2k_2$ daughter mode has disappeared. These observations suggest that saturation mechanisms and nonlinear mode interactions are at play. The emergence of the $k_2 - k_1$ mode, which can only appear when the two modes are initially seeded [27], and the larger amplitude of the k_1 mode indicate that energy is being transferred to the larger scales suggesting the onset of an inverse cascade.

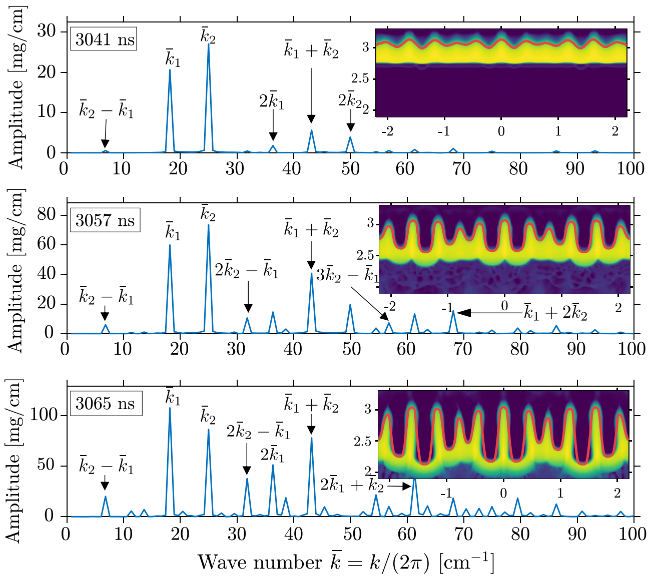

FIG. 4. Fourier spectra of the liner mass per unit length obtained from HYDRA. Inset: simulated density map (in logarithmic scale) of the imploding liner. Horizontal and vertical axes correspond to the axial and radial coordinates, respectively, and are measured in mm. Red lines denote the unfolded contours from the synthetic radiographs in Fig. 2.

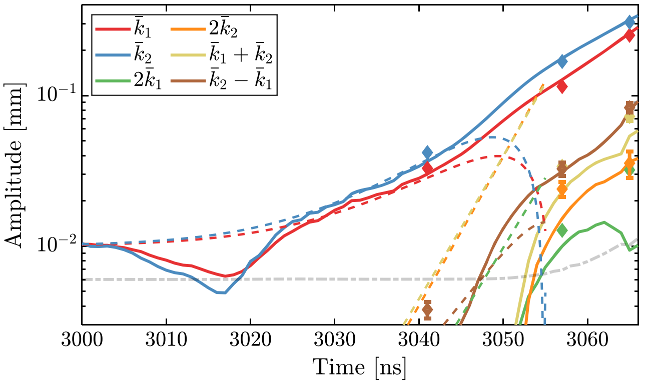

FIG. 5. Time evolution of MRTI amplitudes. Solid lines: LSSA amplitudes of the unfolded contours of the synthetic radiographs. Dashed lines: amplitudes ξ_{k_a} obtained by solving Eqs. (3). Diamonds: LSSA amplitudes of the unfolded contours of the experimental radiographs. Gray dashed line: amplitude that can be measured to better than 30% uncertainty under combined effects of the signal-to-noise ratio, the 15-μm spatial resolution of the diagnostic, the 4.3-μm pixel size of the images, and the LSSA fitting error.

Comparison to weakly nonlinear theory.—The early MRTI growth can be approximately described using the WNL model of Ref. [47] extended to two initially seeded modes. This model considers a single, planar interface separating the plasma fluid and magnetic field. The fluid is assumed perfectly conducting, incompressible, and irrotational. The WNL coupling between the modes k_a belonging to the set $K=\{k_1,k_2,2k_1,2k_2,k_1+k_2,k_2-k_1\}$ can be described by a least action principle $\delta\Lambda=\delta\int_{t_0}^{t_1}L dt=0$. Here, $L\doteq\sum_{k_a\in K}\Phi_{k_a}d\xi_{k_a}/dt-H$ is the Lagrangian of the system, $\xi_{k_a}(t)$ denotes the cosine amplitude of the k_a mode of the outer surface perturbation, and $\Phi_{k_a}(t)$ is the canonical momentum conjugate to ξ_{k_a}. The function $H(t,\xi_{k_a},\Phi_{k_a})$ is the Hamiltonian of the system and is given by

$$
\begin{aligned}
H \doteq{}& \sum_{k_a\in K}\left(\frac{k_a}{2}\Phi_{k_a}^2-\frac{|\ddot{R}|}{2}\xi_{k_a}^2\right)-\frac{k_1^3}{8}\xi_{k_1}^2\Phi_{k_1}^2-\frac{k_2^3}{8}\xi_{k_2}^2\Phi_{k_2}^2\\
&+\frac{1}{2}k_1^2\xi_{2k_1}\Phi_{k_1}^2+\frac{1}{2}k_2^2\xi_{2k_2}\Phi_{k_2}^2\\
&+k_1(k_2-k_1)\xi_{k_2}\Phi_{k_2-k_1}\Phi_{k_1}+k_1k_2\xi_{k_1+k_2}\Phi_{k_1}\Phi_{k_2}\\
&+\frac{1}{4}k_1^2(k_2-k_1)\xi_{k_2}^2\Phi_{k_1}^2-\frac{1}{2}k_1^2k_2\xi_{k_1}\xi_{k_2}\Phi_{k_1}\Phi_{k_2}. \qquad (2)
\end{aligned}
$$

From Eq. (2), we can identify the leading-order interactions between the MRTI modes. The quadratic terms inside the sum correspond to kinetic and potential energies. These terms describe the linear growth of each individual mode [47]. The remaining terms in the first line are nonlinear self-coupling terms for the k_1 and k_2 modes. The terms in the second line couple the k_1 and k_2 modes with their second-harmonic $2k_1$ and $2k_2$ daughter modes. These first nonlinear terms are responsible for the saturation of the mother k_1 and k_2 modes [44–47]. The remaining nonlinear terms represent couplings between the k_1, k_2, k_1+k_2, and k_2-k_1 modes. In particular, the first term in the third line is the main driver for the k_2-k_1 mode. Hamilton's equations are obtained by varying the action Λ with respect to ξ_{k_a} and Φ_{k_a}:

$$
\dot{\xi}_{k_a}=\partial H/\partial\Phi_{k_a}, \qquad \dot{\Phi}_{k_a}=-\partial H/\partial\xi_{k_a}. \qquad (3)
$$

We numerically solved these 12 equations using a fourth-order Runge-Kutta integrator. The liner acceleration $\ddot{R}(t)$ was obtained using a thin-shell model [18,19].

Figure 5 shows the time evolution of the mother and first-generation daughter modes. The experimental points and the simulation results show good agreement. Excluding the ablation phase of the liner surface ($t\simeq 3015$ ns), the WNL model reproduces the early growth of the mother modes until $t\lesssim 3045$ ns. There is also a partial agreement for the amplitude of the k_2-k_1 mode. However, the theory overpredicts the growth of the higher k modes: $2k_1$, k_1+k_2, and $2k_2$. A probable cause is the absent second-generation daughter modes, which can act as energy sinks for the ($2k_1$, k_1+k_2, $2k_2$) modes and limit their growth. Beyond $t\gtrsim 3045$ ns, the mode amplitudes become large causing the WNL perturbation theory to break down. In Fig. 5, this manifests as a sudden change in the mother-mode amplitudes and as an unbounded growth of the higher k modes. This shortcoming of WNL theories cannot be fixed by including additional modes [44–47]. The WNL model also misses cylindrical convergence and feedthrough effects which become important as the liner further implodes [49,50]. Adding these effects into a nonlinear analytical framework could improve our understanding of MRTI.

Conclusions.—We conducted experiments to study the MRTI with two initially seeded modes. Using a novel technique to uncover the underlying transmission contours of the radiographs with the ±3° viewing angle removed, we showed experimental evidence of harmonic generation and the onset of an inverse cascade resulting from the nonlinear coupling of discrete modes. These experimental findings agreed well with predictions from HYDRA simulations. We presented a weakly nonlinear model that identifies the leading-order nonlinear interactions between the MRTI modes. Before breakdown, the model reproduces the dynamics of the largest-amplitude modes, but the model shows disagreement for the lowest-amplitude modes.

These findings motivate new controlled experiments to scope the inverse cascade of MRTI in a deeper nonlinear regime. Seeding more discrete axial modes (with well-characterized initial amplitudes) can increase the number of nonlinear interactions. A new multiframe radiography diagnostic with a 0° viewing angle would remove the shadowing of the MRTI features and simplify data analysis. From the theory side, the techniques in Ref. [51] can be used to quantify the dominant energy-transfer mechanisms occurring in cylindrical MRTI, e.g., the kinetic-to-kinetic and magnetic-to-kinetic energy-transfer channels. Developing new analytical theories for describing fully nonlinear, multimode MRTI is left for future work.

We thank the Z, Z-Beamlet, diagnostics, target, and hardware teams for their support of this work. D. E. R. was partially supported by the Sandia National Laboratories (SNL) Truman Fellowship in National Security Science and Engineering, which is part of the LDRD Program, Project No. 209289. SNL is a multimission laboratory managed and operated by National Technology & Engineering Solutions of Sandia, LLC, a wholly owned subsidiary of Honeywell International Inc., for the U.S. Department of Energy's National Nuclear Security Administration under Contract No. DE-NA0003525. This Letter describes objective technical results and analysis. Any subjective views or opinions that might be expressed in the paper do not necessarily represent the views of the U.S. Department of Energy or the U.S. Government.

---

[*] Corresponding author.
deruiz@sandia.gov

[1] S. Chandrasekhar, *Hydrodynamic and Hydromagnetic Stability* (Oxford University Press, London, 1961).

[2] M. D. Kruskal and M. Schwarzschild, Proc. R. Soc. A **223**, 348 (1954).

[3] J. M. Stone and T. Gardiner, Astrophys. J. **671**, 1726 (2007).

[4] A. S. Hillier, Mon. Not. R. Astron. Soc. **462**, 2256 (2016).

[5] A. S. Hillier, T. Berger, H. Isobe, and K. Shibata, Astrophys. J. **746**, 120 (2012).

[6] H. Isobe, T. Miyagoshi, K. Shibata, and T. Yokoyama, Nature (London) **434**, 478 (2005).

[7] J. J. Hester, J. M. Stone, P. A. Scowen, B.-I. Jun, J. S. I. Gallagher, M. L. Norman, G. E. Ballester, C. J. Burrows, S. Casertano, J. T. Clarke *et al.*, Astrophys. J. **456**, 225 (1996).

[8] O. Porth, S. S. Komissavorv, and R. Keppens, Mon. Not. R. Astron. Soc. **443**, 547 (2014).

[9] M. K. Matzen, C. Deeney, R. J. Leeper, J. L. Porter, R. B. Spielman, G. A. Chandler, M. S. Derzon, M. R. Douglas, D. L. Fehl, D. E. Hebron *et al.*, Plasma Phys. Controlled Fusion **41**, A175 (1999).

[10] D. D. Ryutov, M. S. Derzon, and M. K. Matzen, Rev. Mod. Phys. **72**, 167 (2000).

[11] D. B. Sinars, M. A. Sweeney, C. S. Alexander, D. J. Ampleford, T. Ao, J. P. Apruzese, C. Aragon, D. J. Armstrong, K. N. Austin, T. J. Awe *et al.*, Phys. Plasmas **27**, 070501 (2020).

[12] E. G. Harris, Phys. Fluids **5**, 1057 (1962).

[13] S. A. Slutz, M. C. Herrmann, R. A. Vesey, A. B. Sefkow, D. B. Sinars, D. C. Rovang, K. J. Peterson, and M. E. Cuneo, Phys. Plasmas **17**, 056303 (2010).

[14] M. R. Gomez, S. A. Slutz, A. B. Sefkow, D. B. Sinars, K. D. Hahn, S. B. Hansen, E. C. Harding, P. F. Knapp, P. F. Schmit, C. A. Jennings *et al.*, Phys. Rev. Lett. **113**, 155003 (2014).

[15] M. R. Gomez, S. A. Slutz, C. A. Jennings, D. J. Ampleford, M. R. Weis, C. E. Myers, D. A. Yager-Elorriaga, K. D. Hahn, S. B. Hansen, E. C. Harding *et al.*, Phys. Rev. Lett. **125**, 155002 (2020).

[16] D. A. Yager-Elorriaga, M. R. Gomez, D. E. Ruiz, S. A. Slutz, A. J. Harvey-Thompson, C. A. Jennings, P. F. Knapp, P. F. Schmit, M. R. Weis, T. J. Awe *et al.*, Nucl. Fusion. **62**, 042015 (2022).

[17] P. F. Knapp, M. R. Martin, D. H. Dolan, K. Cochrane, D. Dalton, J. P. Davis, C. A. Jennings, G. P. Loisel, D. H. Romero, I. C. Smith *et al.*, Phys. Plasmas **24**, 042708 (2017).

[18] D. B. Sinars, S. A. Slutz, M. C. Herrmann, R. D. McBride, M. E. Cuneo, K. J. Peterson, R. A. Vesey, C. Nakhleh, B. E. Blue, K. Killebrew *et al.*, Phys. Rev. Lett. **105**, 185001 (2010).

[19] D. B. Sinars, S. A. Slutz, M. C. Herrmann, R. D. McBride, M. E. Cuneo, C. A. Jennings, J. P. Chittenden, A. L. Velikovich, K. J. Peterson, R. A. Vesey *et al.*, Phys. Plasmas **18**, 056301 (2011).

[20] R. D. McBride, M. R. Martin, R. W. Lemke, J. B. Greenly, C. A. Jennings, D. C. Rovang, D. B. Sinars, M. E. Cuneo, M. C. Herrmann, S. A. Slutz *et al.*, Phys. Plasmas **20**, 056309 (2013).

[21] T. J. Awe, K. J. Peterson, E. P. Yu, R. D. McBride, D. B. Sinars, M. R. Gomez, C. A. Jennings, M. R. Martin, S. E. Rosenthal, D. G. Schroen, A. B. Sefkow, S. A. Slutz, K. Tomlinson, and R. A. Vesey, Phys. Rev. Lett. **116**, 065001 (2016).

[22] J. C. Zier, R. M. Gilgenbach, D. A. Chalenski, Y. Y. Lau, D. M. French, M. R. Gomez, S. G. Patel, I. M. Rittersdorf,

A. M. Steiner, M. Weis *et al.*, Phys. Plasmas **19**, 032701 (2012).
[23] T. J. Awe, R. D. McBride, C. A. Jennings, D. C. Lamppa, M. R. Martin, D. C. Rovang, S. A. Slutz, M. E. Cuneo, A. C. Owen, D. B. Sinars *et al.*, Phys. Rev. Lett. **111**, 235005 (2013).
[24] T. J. Awe, C. A. Jennings, R. D. McBride, M. E. Cuneo, D. C. Lamppa, M. R. Martin, D. C. Rovang, D. B. Sinars, S. A. Slutz, A. C. Owen *et al.*, Phys. Plasmas **21**, 056303 (2014).
[25] D. A. Yager-Elorriaga, P. Zhang, A. M. Steiner, N. M. Jordan, P. C. Campbell, Y. Y. Lau, and R. M. Gilgenbach, Phys. Plasmas **23**, 124502 (2016).
[26] D. A. Yager-Elorriaga, Y. Y. Lau, P. Zhang, P. C. Campbell, A. M. Steiner, N. M. Jordan, R. D. McBride, and R. M. Gilgenbach, Phys. Plasmas **25**, 056307 (2018).
[27] M. R. Douglas, C. Deeney, and N. F. Roderick, Phys. Plasmas **5**, 4183 (1998).
[28] M. M. Marinak, R. E. Tipton, O. L. Landen, T. J. Murphy, P. Amendt, S. W. Haan, S. P. Hatchett, C. J. Keane, R. McEachern, and R. Wallace, Phys. Plasmas **3**, 2070 (1996).
[29] J. M. Koning, G. D. Kerbel, and M. M. Marinak, The HYDRA magnetohydrodynamics package, in *APS Meeting Abstracts* (2014), https://ui.adsabs.harvard.edu/abs/2009APS..DPPNP8101K.
[30] G. R. Bennett, I. C. Smith, J. E. Shores, D. B. Sinars, G. Robertson, B. W. Atherton, M. C. Jones, and J. L. Porter, Rev. Sci. Instrum. **79**, 10E914 (2008).
[31] A. B. Sefkow, S. A. Slutz, J. M. Koning, M. M. Marinak, K. J. Peterson, D. B. Sinars, and R. A. Vesey, Phys. Plasmas **21**, 072711 (2014).
[32] A. J. Harvey-Thompson, M. R. Weis, E. C. Harding, M. Geissel, D. J. Ampleford, G. A. Chandler, J. R. Fein, M. E. Glinsky, M. R. Gomez, K. D. Hahn *et al.*, Phys. Plasmas **25**, 112705 (2018).
[33] M. R. Weis, A. J. Harvey-Thompson, and D. E. Ruiz, Phys. Plasmas **28**, 012705 (2021).
[34] R. M. More, K. H. Warren, D. A. Young, and G. B. Zimmerman, Phys. Fluids **31**, 3059 (1988).
[35] M. P. Desjarlais, Contrib. Plasma Phys. **41**, 267 (2001).
[36] T. J. Awe, E. P. Yu, M. W. Hatch, T. M. Hutchinson, K. Tomlinson, W. D. Tatum, K. C. Yates, B. T. Hutsel, and B. S. Bauer, Phys. Plasmas **28**, 072104 (2021).
[37] V. I. Oreshkin, Phys. Plasmas **15**, 092103 (2008).
[38] K. J. Peterson, D. B. Sinars, E. P. Yu, M. C. Herrmann, M. E. Cuneo, S. A. Slutz, I. C. Smith, B. W. Atherton, M. D. Knudson, and C. Nakhleh, Phys. Plasmas **19**, 092701 (2012).
[39] K. J. Peterson, E. P. Yu, D. B. Sinars, M. E. Cuneo, S. A. Slutz, J. M. Koning, M. M. Marinak, C. Nakhleh, and M. C. Herrmann, Phys. Plasmas **20**, 056305 (2013).
[40] K. J. Peterson, T. J. Awe, E. P. Yu, D. B. Sinars, E. S. Field, M. E. Cuneo, M. C. Herrmann, M. Savage, D. Schroen, K. Tomlinson, and C. Nakhleh, Phys. Rev. Lett. **112**, 135002 (2014).
[41] E. P. Yu, T. J. Awe, K. R. Cochrane, K. C. Yates, T. M. Hutchinson, K. J. Peterson, and B. S. Bauer, Phys. Plasmas **27**, 052703 (2020).
[42] C. I. Puryear, O. N. Portniaguine, C. M. Cobos, and J. P. Castagna, Geophysics **77**, V143 (2012).
[43] We preferred the LSSA method over the traditional fast Fourier transform, as it led to cleaner spectra, which then facilitated the interpretation of the new MRTI modes emerging from nonlinear interactions.
[44] R. L. Ingraham, Proc. Phys. Soc. B **67**, 748 (1954).
[45] J. W. Jacobs and I. Catton, J. Fluid Mech. **187**, 329 (1988).
[46] M. Berning and A. M. Rubenchik, Phys. Fluids **10**, 1564 (1998).
[47] D. E. Ruiz, Phys. Plasmas **27**, 022121 (2020).
[48] The initial amplitude is estimated using $\delta\hat{m}_0 \simeq 2\pi\rho_0 R_0 A_0[\cos(k_1 z) + \cos(k_2 z)]$, where $\rho_0 = 2.7\ \mathrm{g/cm^3}$. This gives an amplitude of $2\pi\rho_0 R_0 A_0 \simeq 5.34\ \mathrm{mg/cm}$.
[49] M. R. Weis, P. Zhang, Y. Y. Lau, P. F. Schmit, K. J. Peterson, M. Hess, and R. M. Gilgenbach, Phys. Plasmas **22**, 032706 (2015).
[50] A. L. Velikovich and P. F. Schmit, Phys. Plasmas **22**, 122711 (2015).
[51] P. Grete, B. W. O'Shea, K. Beckwith, W. Schmidt, and A. Christlieb, Phys. Plasmas **24**, 092311 (2017).